Thesis for the degree of Licentiate of Engineering Physics

Direct conversion of methane-to-methanol in Cu-exchanged small-pore zeolites

First-principles calculations

Unni Engedahl

CHALMERS

Department of Physics

Chalmers University of Technology

Gothenburg, Sweden 2020

Direct conversion of methane-to-methanol in Cu-exchanged small-pore zeolites
First-principles calculations
Unni Engedahl

Department of Physics
Chalmers University of Technology
SE-412 96 Gothenburg
Sweden
Telephone: +46 (0)31-772 1000

Cover:
Methane is converted into methanol inside the zeolite framework of Cu-SSZ-13.

Printed at Chalmers Digitaltryck
Gothenburg, Sweden 2020

Direct conversion of methane-to-methanol in Cu-exchanged small-pore zeolites
First-principles calculations

Unni Engedahl
Department of Physics
Chalmers University of Technology

Abstract

Fossil fuel consumption continuous to increase world wide and of all the fossil fuels, natural gas is growing the most. The combustion of natural gas, which mainly contains methane, is more environmental friendly than oil or coal thanks to its high specific energy. More energy gained and less CO_2 released per kg fuel motivates the increased production. This in turn increases the demand on manageability, resulting in the practice of liquefying natural gas. The gas is kept in liquid form, via high pressure or low temperature, for transport and distribution. In an effort to reduce the energy cost of managing gaseous energy resources, the conversion of methane into its liquid counterpart methanol is highly desired. The established procedure for the conversion is a large scale, multi-step, power-plant process, and there is a need for a small scale, direct conversion alternative. Copper-exchanged zeolites are considered promising candidates for the methane-to-methanol reaction, where mono-, dimer, and trimer Cu-clusters have been suggested to be the active site.

In this thesis, the catalytic properties of Cu-dimers in zeolites are studied using first-principles calculations, ab initio thermodynamics, and micro kinetic modeling. As a first step, the stability of the Cu-dimer structure in SSZ-13 is investigated under direct conversion conditions. The zeolite is found to be very humid and the structure of the proposed active site highly dependent on temperature and partial pressure of relevant gases. Under reaction conditions, the Cu_2O and Cu_2OH structures are found to be the energetically most preferred. Performing the direct conversion over the identified active sites reveals a low activity for the reaction, stemming from a high free energy barrier of the C-H bond in methane and an inability for methanol to desorb. The activity of the Cu_2O site is, however, increased when water is added into the reaction mechanism. Presence of water enables desorption of the reaction products and results in an endergonic reaction path. The Cu_2OH site responds in the opposite manner with respect to water, becoming less active. The new insights on the nature of the active site and the reaction mechanism provide a deeper understanding, which will aid the future search for new catalytic materials with high activity and selectivity.

Keywords: partial methane oxidation, density functional theory, micro-kinetic modeling, zeolites, CHA, SSZ-13, copper

List of Publications

This thesis is based on the following appended papers:

Paper I

First-Principles Study of Oxidation State and Coordination of Cu-Dimers in Cu-SSZ-13 During Methane-to-Methanol Reaction Conditions

U. Engedahl, H. Grönbeck, and A. Hellman

Journal of Physical Chemistry C. Vol. 123 (43), p. 26145-26150

Paper II

Reaction Mechanism for Methane-to-Methanol in Cu-SSZ-13: First-Principles Study of the $Z_2[Cu_2O]$ and $Z_2[Cu_2OH]$ Motifs in the Small-Pore Zeolite Chabazite

U. Engedahl, A. A. Arvidsson, H. Grönbeck, and A. Hellman

In manuscript

My contributions to the publications

Paper I

I performed all calculations and co-authored the paper.

Paper II

I performed all DFT calculations and co-authored the paper.

Contents

Chapter 1

Introduction

Approximately 25% of the fuel consumed in the world during 2019 was in the form of natural gas, a number that is projected to increase over the coming years [1]. With an increasing use of 1.1% yearly (compared with liquids' 0.6% per year growth and coal's 0.4% per year growth), natural gas is the world's fastest growing fossil fuel [1]. The increasing consumption is driven by an expanding industrial sector and a replacement of coal with methane in electricity generation [1].

Natural gas is comprised mainly of methane, which has a higher specific energy (Wh per kg) than any other hydrocarbons thanks to its high carbon-to-hydrogen ratio [2]. This does not only mean more energy gained upon combustion, but also less CO_2 released per combusted kilogram of the fuel. However, methane is a gas and, thus, precarious to store and distribute. Although not toxic, it is highly flammable and a potent greenhouse gas. Thus, leakage or partial combustion is a potential danger, both in the short and long term. A better utilisation of methane resources would be possible if it was converted into a liquid. Today, liquification of natural gas (LNG) is done at very high pressure (850 kPa at room temperature) or low temperature (-162°C) [3]. To save the energy spent in liquefying methane, the same safety and convenience effects could be reached by converting methane into its liquid counterpart, i.e. methanol.

Industrial transformation of methane to methanol is performed over a $Cu/ZnO/Al_2O_3$ catalyst [4] in two steps: conversion of methane into syngas at high temperature, from which CO and H_2 is converted into CH_3OH and H_2O over a catalyst surface at high pressure [5]. The process is highly energy demanding and partly results in unwanted bi-products of CO_2 and H_2O. Furthermore, it is a power plant process; the technology needs large scale production to be economically feasible. A cost and energy effective alternative to this large scale process would be direct conversion of methane. Partial oxidation of methane over a highly selective catalyst performed at low temperature would enable small scale, maybe even portable, use. However, this process needs a catalytic material not yet identified.

1.1 Catalysis

Catalysis is a phenomena in which the rate of a chemical reaction is increased by addition of a catalyst. A catalytic material is a material that aids and promotes a reaction without being consumed. Enhancing the rate of a reaction is a two-fold problem. The activity of the reaction should increase while the selectivity towards the desired product is maintained.

By adding a catalyst, the reaction is directed into a more complex, but energetically more favourable reaction path, leading to an increase in activity. Depending on the reaction path, the catalyst can also control the selectivity to the desired product. An example of a catalyzed reaction is illustrated in fig. 1.1.

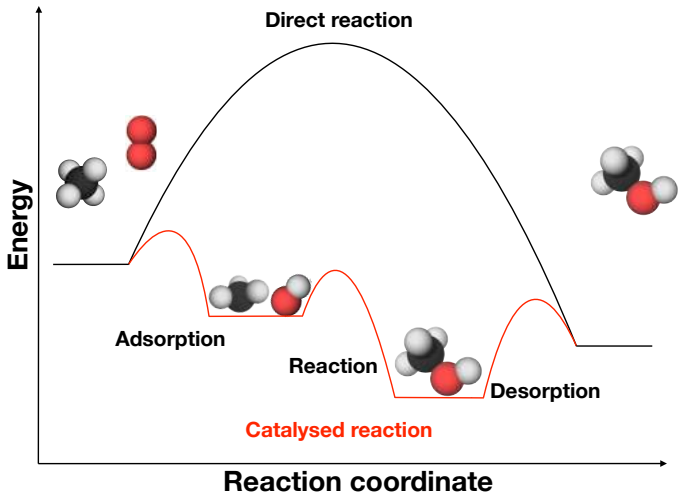

Figure 1.1: The purpose of catalysis is to increase the rate of a desired reaction. By diverting the reaction into a path which divides the process into several steps, the new energy barrier for the reaction to occur is lower than that of the uncatalyzed reaction.

By forming new bonds with the reactants, the catalyst is able to break existing bonds and provide a lower energy barrier for the reaction to take place. For this to happen, the catalyst should follow the Sabatier's principle [7, 6]. If the bonds between the catalyst and the reactants are too weak, the coverage of the reactants will be too low and the barrier too high, resulting in a low conversion. If the bond between the catalyst and any of the intermediate steps in the reaction is too strong, the reaction will not be able to proceed, and the catalyst will become poisoned. Importantly, a catalyst only changes the kinetics of a reaction, it does not affect the thermodynamics. If the reaction is thermodynamically unfavourable without a catalyst, it will continue to be so in the presence of a catalyst.

The two main catalyst categories are homogeneous and heterogeneous catalysts. A homogeneous catalyst is a catalyst existing in the same phase as the reactants and products, e.g. a liquid promoting a liquid reaction. A heterogeneous catalyst is a catalyst existing in a different phase than the reactants, e.g. a solid surface promoting a gaseous reaction. The site on which the reaction takes place is called an active site [8]. This can be a small cluster or an atom that has a different structure and composition as compared to the surrounding material. Controlling the structure and composition of this active site influences the catalytic properties of the material. One important aspect of the catalytic properties is the interplay between activity and selectivity. For instance, increasing

activity of a reaction does not necessarily mean that selectivity is maintained. The most selective catalysts are enzymes, able to produce almost exclusively the desired product. This type of naturally occurring (often protein based) catalyst is called a biocatalyst. In a biocatalyst there is a geometric component that influences the selectivity; like a puzzle where only the correct piece fits, only one reaction is promoted. Although these catalysts are selective, the activity is generally low. On, for instance, an extended surface catalyst, where this geometric featured is missing or less pronounced, this same effect might be difficult to achieve. However, it might be formed during reaction conditions, by the adsorbate coverage. A catalytic material with porous structure has the additional effects of confinement. Where, the selectivity might then be controlled by the catalysts ability to act as a sieve, in addition to the properties given by the active sites.

1.2 Methane to methanol conversion in zeolites

Drawing inspiration from nature and naturally occurring biocatalysts is helpful when designing more selective catalytic materials. One example of this is enzymatic methane monooxygenases (MMOs)[9, 10]. On the sparse metal sites in the porous protein structure, methane is converted into methanol with a very high selectivity, but (for industrial use) too low activity. In an effort to mimic this very selective process and increase the rate of the reaction, metal ion-exchanged zeotypes (then called zeolites), systems with a similarly porous structure and the possibility of single active sites (as seen in fig. 1.2), are being investigated.

A zeotype is a porous material comprised of corner-sharing SiO_4 tetrahedrons, or T-sites. Owing to the flexibility of how these primitive building-blocks can be connected, there are more than 200 confirmed structures [12] with different porosity. The pore sizes, ranging from 4 to 12 membered rings (MRs), is a way to control the accessibility in the material. By replacing an Si^{4+} for an ion of either lower or higher charge, the otherwise chemically inert framework becomes prone to catalytic reactions and the acidity of the structure is changed. If substituting Al^{3+} into the framework, the structure is called zeolite. The introduced charge deficit must be compensated by the insertion of cations, like H^+, Na^+, or Cu^+. The concentration and relative position of the framework Al^{3+} and the choice of cation contributes to the characteristics of the zeolite catalyst [13].

Two of the zeolite structures studied for the partial oxidation reaction are called ZSM-5 and SSZ-13. The MFI structure of ZSM-5 has 4, 5, 6, and 10 MRs, where the odd MRs gives the structure channels. The smaller chabazite structure SSZ-13 is made up of 4, 6, and 8 MRs, connected to form a network comprised of one small and one large cage, as seen in fig. 1.2. In the MMO, the active sites are spares metal atom sites. Zeolites, ion-exchange with metal atoms such as iron and copper, have shown the same ability to convert methane to methanol [14, 15, 17, 16]. However, the specific structure of these metal-ion sites in the catalyst is still under debate.

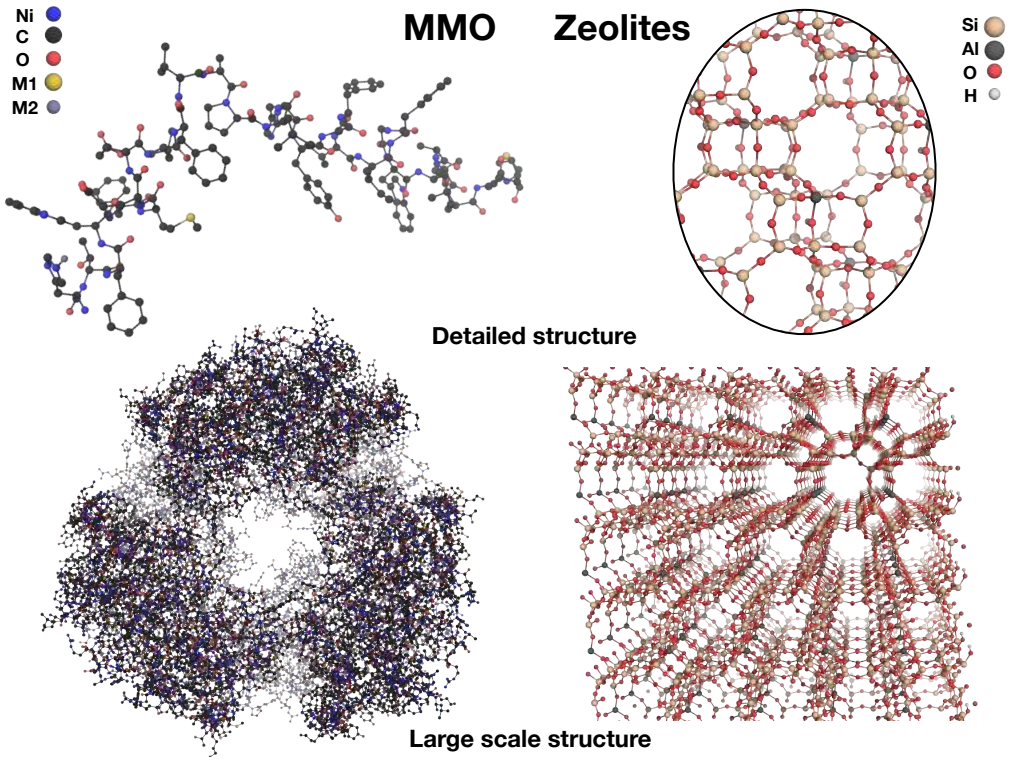

Figure 1.2: The protein responsible for biological oxidation of methane, MMO [11], along side the zeolite structure of SSZ-13. The structures are similar, both on a small and a large scale, having a porous structure and the possibility of single, metal atom sites. MMO is composed of carbon, nitrogen, oxygen, and sparse metal sites (here denoted M1 and M2); the components of the zeolites are silicon, aluminium, oxygen, and the possibility of charge compensating metal sites (here represented by protons).

1.3 Objective

This thesis has two aims. The first is to investigate and determine the coordination and oxidation state of the $[\text{Cu-O-Cu}]^{2+}$ motif in copper exchanged SSZ-13 during the conditions of direct methane-to-methanol conversion. The second is to explore the reaction mechanism for the partial oxidation over the relevant active sites. This is explored using computational methods, in particular density functional theory (DFT), ab initio thermodynamics, and micro kinetic modeling.

Chapter 2

Electronic structure calculations

Investigating the catalytic potential of an atomic system means that the physical and chemical properties of the material should be determined. From a theoretical and computational point of view, this can be done by studying the electronic structure of the system. Systems of a single electron (i.e. H or He^+) can be solved exactly from the Schrödinger (or Dirac) equation. However, systems with more electrons are complex and an exact solution of the many-body wave function very quickly becomes unattainable. As such, a method is required for gaining the desired electronic structure of the system, while circumventing the need to solve the full Schrödinger equation.

2.1 Many-body systems

The complete description of a many-body atomic system comprised of N electrons with charge $-e$, and K nuclei with charge $Z_I e$, is given by the Hamiltonian [18],

$$\begin{aligned}\hat{H} = &-\sum_{i}^{N}\frac{\hbar^2}{2m_e}\nabla_i^2 - \sum_{I}^{K}\frac{\hbar^2}{2M_I}\nabla_I^2 + \frac{1}{4\pi\epsilon_0}\sum_{i}^{N}\sum_{j>i}^{N}\frac{e^2}{|\mathbf{r}_i - \mathbf{r}_j|} \\ &-\frac{1}{4\pi\epsilon_0}\sum_{I}^{K}\sum_{i}^{N}\frac{Z_I e^2}{|\mathbf{r}_i - \mathbf{R}_I|} + \frac{1}{4\pi\epsilon_0}\sum_{I}^{K}\sum_{J>I}^{K}\frac{Z_I Z_J e^2}{|\mathbf{R}_I - \mathbf{R}_J|}\end{aligned} \tag{2.1}$$

where the basic components are the kinetic and potential energy of the system, more specifically:

$$T = -\sum_{i}^{N}\frac{\hbar^2}{2m_e}\nabla_i^2 - \sum_{I}^{K}\frac{\hbar^2}{2M_I}\nabla_I^2 \qquad \text{kinetic energy}$$

$$V_{el} = \frac{1}{4\pi\epsilon_0}\sum_{i}^{N}\sum_{j>i}^{N}\frac{e^2}{|\mathbf{r}_i - \mathbf{r}_j|} \qquad \text{electron-electron interaction}$$

$$V_{el-nuc} = -\frac{1}{4\pi\epsilon_0}\sum_{I}^{K}\sum_{i}^{N}\frac{Z_I e^2}{|\mathbf{r}_i - \mathbf{R}_I|} \qquad \text{electron-nuclei interaction}$$

$$V_{nuc} = \frac{1}{4\pi\epsilon_0}\sum_{I}^{K}\sum_{J>I}^{K}\frac{Z_I Z_J e^2}{|\mathbf{R}_I - \mathbf{R}_J|} \qquad \text{nuclei-nuclei interaction.}$$

To be able to solve the Schrödinger equation, $\hat{H}\Psi = E\Psi$, for any but the most elementary systems, the first step is to assume that the electronic and ionic part of the wave function are independent of each other and can be separated, i.e. $\Psi_{tot}(\mathbf{r}, \mathbf{R}) = \Psi_{el}(\mathbf{r}, \mathbf{R})\Psi_{nuc}(\mathbf{R})$. This ansatz is called the Born-Oppenheimer approximation [19]. This can be understood as the electrons instantaneously adapting to changes in the nuclei positions while remaining in their stationery state. The electronic wave function is, thus, decoupled from the nuclei, which is fixed at position $\mathbf{R}$, where any crossterm between Ψ_{el} and Ψ_{nuc} is ignored. The electron-nucleic interaction is considered as an external potential, and the electronic Hamiltonian becomes

$$\hat{H}_{el} = T + V_{el} + V_{el-nuc}. \tag{2.2}$$

The Coulomb attraction between the electrons and nuclei, described in the electron-nuclei interaction term, V_{el-nuc} will now be referred to as an external potential V_{ext}.

Though decoupled from the nuclei, the electronic Schrödinger equation formed using eq. (2.2) is still very computationally expensive. The description possesses one major obstacle, namely the wave function's dependence on the particle positions $\Psi(\mathbf{r}_1 ... \mathbf{r}_N, \mathbf{R})$; the dimensionality of the Schrödinger equation is proportional to the number of electrons in the system. Thus, with increasing system size, solving the Schrödinger equation becomes an insurmountable task.

2.2 Density functional theory

Chronologically, the first method for circumventing the difficulties with the many-body wave function was the Hartree-Fock method [20, 21, 22]. By approximating the electronic many-body wave function with a Slater determinant [23] constructed from one-electron wave functions, the anti-symmetry of a fermionic system is enforced. All interaction that is not included in this spin-interaction (from now on called exchange) is referred to as correlation, and is completely neglected.

In 1964, two theorems devised by Hohenberg and Kohn layed the foundation for a way of handling the atomic system with both accuracy and a smaller computational effort. The two theorems tell us to relinquish the idea of solving the wave function and that instead the electron density could be considered [24]. The theorems states that: (1) when in any external potential, V_{ext}, the total energy of a system is a functional of the electronic density

$$E[n(\mathbf{r})] = \int d\mathbf{r} V_{ext}(\mathbf{r}) n(\mathbf{r}) + F[n(\mathbf{r})], \tag{2.3}$$

and (2) the ground state of the system is determined by the global minimum value of eq. (2.3) [25]. Thus, using the electron density, $n(\mathbf{r}) = |\Psi|^2$, a function of three spatial coordinates can replace the myriad of electronic positions in a many-body wave function of the system.The energy of the system is now a function of the electron density, which is a function of positions, a function of a function or a *functional*, a density functional.

2.2.1 Kohn-Sham orbitals - A non-interacting representation

The introduced universal functional $F[n(\mathbf{r})]$ on the right hand side in eq. (2.3) contains the individual contributions of the kinetic energy, the classic Coulomb interaction (or Hartree energy, E_H), and the non-classical interactions of the electrons (or exchange-correlation energy, $\widetilde{E}_{xc}$),

$$E[n(\mathbf{r})] = T[n(\mathbf{r})] + \int d\mathbf{r} V_{ext}[n(\mathbf{r})]n(\mathbf{r}) + E_H[n(\mathbf{r})] + \widetilde{E}_{xc}[n(\mathbf{r})]. \tag{2.4}$$

The Hartree term in eq. (2.4) contains an unphysical self-interaction error as the electron interacts with all other electrons in the system, including itself. This error should be completely canceled by the exchange-correlation term, $\widetilde{E}_{xc}$.

Another challenge is that the exact form of the kinetic functional is not known. Kohn-Sham solves this problem by introducing a non-interacting system and allow the exchange-correlation term, E_{xc}, to compensate also for this ansatz. This fictitious non-interacting system generates the same electron ground state density as the given system of interacting particles, and thus the same ground state energy,

$$E[n(\mathbf{r})] = \sum_i^n \epsilon_i - \int d\mathbf{r} V_{ext}[n(\mathbf{r})]n(\mathbf{r}) - E_H[n(\mathbf{r})] + E_{xc}[n(\mathbf{r})]. \tag{2.5}$$

E_{xc} should account for $T - T_0$, which is the difference between the true kinetic energy of the system and that of the non-interacting system. In eq. (2.5), ϵ_i are the Kohn-Sham energies of the non-interacting system.

The Kohn-Sham decomposition effectively separates the terms in the functional that are possible to solve from those that are not. Using atomic units ($e = \hbar = m_e = \frac{1}{4\pi\epsilon_0} = 1$), the Kohn-Sham equations of this model system becomes

$$\left(-\frac{1}{2}\nabla^2 + v_{ext}(\mathbf{r}) + v_H(\mathbf{r}) + v_{xc}(\mathbf{r})\right)\psi_i(\mathbf{r}) = \epsilon_i\psi_i(\mathbf{r}). \tag{2.6}$$

Solving these Kohn-Sham equations in a self-consistent field manner results in the systems density and energy. The problem is that the exact form of the exchange-correlation interaction remains unknown. This means that DFT is an exact theory, given the exact exchange-correlation energy. The accuracy is, in principle, given by the approximation of the exchange-correlation term in eq. (2.5).

2.2.2 Exchange-correlation approximations

The exchange-correlation energy, $E_{xc}[n(\mathbf{r})]$, can be interpreted as the Coulomb interaction between the electronic density and a positively charges "hole" around the electron caused by the Pauli and Coulomb repulsion [26]. This hole represents a fictitious charge depletion around the electron where the likelihood for finding a second electron is greatly reduced. How to model this charge depletion is a matter of approximations.

LDA - Local density approximation

The LDA [27, 24] is an approximation which is solely dependent on the local electron density, and is expressed according to,

$$E_{xc}[n(\mathbf{r})] = \int d\mathbf{r} n(\mathbf{r}) \epsilon_{xc}^{LDA}[n(\mathbf{r}), \mathbf{r}]. \tag{2.7}$$

This can be extended into a Local Spin-Density Approximation (LSDA)[28, 29], taking the electron spin into account. For LDA to be sufficient, the electron density must vary sufficiently slow, such as in the homogeneous electron gas or simple metal-like systems. The LDA generally overbinds, producing too short bonds and too small lattice parameters [30]. In addition, it also performs poorly when modeling strongly correlated systems, such as transition metal oxides [31].

GGA - Generalized gradient approximation

Including a dependence on the change in electron density via an exchange-correlation enhancement factor F_{xc}, a semi-local approximation that improves on the LDA and LSDA called the generalized gradient approximation (GGA) [32, 33], is formed. This expression looks like,

$$E_{xc}^{GGA}[n(\mathbf{r})] = \int d\mathbf{r} n(\mathbf{r}) \epsilon_{xc}^{LDA}[n(\mathbf{r})] F_{xc}[n(\mathbf{r}), \nabla n(\mathbf{r})]. \tag{2.8}$$

GGA functionals outperform L(S)DA when it comes to over-binding, and in many cases predict the lattice constants closer to experimental values. However, just as LDA, it performs poorly for strongly correlated systems [31].

Hybrid functionals - Beyond first-principles

When it comes to strongly correlated systems, one way to improve on GGA is to include the exact exchange energy of Hartree-Fock, E_x^{HF}, into the functional

$$E_{xc}^{hyb} = \alpha E_x^{HF} + (1 - \alpha) E_x^{DFT} + E_c^{DFT}. \tag{2.9}$$

In this, so called, hybrid functional [34], E_x^{DFT} and E_c^{DFT} are the exchange and correlation parts of the density functional, calculated with a chosen GGA functional. This mixing of exact and approximated exchange energies enables the approximation to improve the calculation of properties for which LDA and GGA are not sufficient. The value of the constant α in eq. (2.9) is often chosen after fitting against experimental data sets [34, 35], resulting in the effect that one choice of α might suit one particular type of system better than another.

van der Waals interaction

One correlation effect that LDA, GGA, and hybrid functionals does not account for properly, is the long range interaction (also called dispersion interaction or van der Waals interaction) that exists between systems without overlapping charge densities. It is commonly explained as an instantaneous dipole moment on one system inducing a dipole moment on the other, the attraction between these dipole moments results in an interaction which, in the limit of large separation R, has the behaviour

$$E_{dist} = -\frac{C_6}{R^6}, \tag{2.10}$$

where C_6 is a dispersion coefficient whose value depends on the systems involved. One method for calculating the interaction is determining the C_6 coefficient. This can be done empirically or semi-empirically [36, 37, 38, 39]. Another approach is basing the interaction on the adiabatic connection [40], an exact expression for the exchange-correlation energy in terms of electron–electron repulsion [41]. This results in a non-local expression involving the density at two different points [42, 43, 44]. This allows for including vdW-interaction self-consistently in DFT.

2.2.3 Solving the Kohn-Sham equation

After choosing an exchange-correlation approximation, the more practical task of solving the Kohn-Sham equation remains. Depending on the nature of the system, the sought after information, and the computational resources, different approaches are appropriate.

One approach is to expand the Kohn-Sham orbitals in a linear combination of atomic orbitals (LCAO) [45],

$$\psi_i(\mathbf{r}) = \sum_j c_{ij}\chi_j(\mathbf{r}) \tag{2.11}$$

where $\psi_i(\mathbf{r})$ are the Kohn-Sham one-electron orbitals of eq. (2.6) and $\chi_j(\mathbf{r})$ are the chosen basis set. Here, c_{ij} are coefficients determined self-consistently through minimising the energy in eq. (2.6). This approach makes calculations considerably cheap, although the accuracy will be limited by the quality of the chosen basis.

If periodic boundary conditions are applied to the system, a plane wave basis is suitable due to its inherent periodic nature,

$$\psi_j(\mathbf{r}) = \sum_{\mathbf{k}} c_{j\mathbf{k}} e^{i\mathbf{k}\cdot\mathbf{r}}. \tag{2.12}$$

The series is truncated such that the kinetic energy of the plane waves is lower than a specified cut off energy, $\frac{\hbar^2 k^2}{2m_e} < E_{cut}$. A higher E_{cut} includes more rapidly changing features in the calculation resulting in a more accurate description of the system, but at a higher computational cost.

Treatment of core electrons - Pseudopotentials and PAW

Rapidly changing orbitals of the core electrons cannot in a practical manner be represented by a plane wave basis set. This problem is mended by e.g. the use of pseudopotentials [46]. Assuming a frozen core approximation [47], in which the core states are assumed to be unaffected by the ion's environment, the pseudopotentials model the core electrons by an effective potential, treating the behaviour of the core separately for that of the valence. Since the valence electrons describe the chemical behaviour of a system, this separate treatment of the core is often appropriate when bonding and rehybridization are investigated. The Vienna Ab initio Simulation Package (VASP) [48, 49, 50, 51, 52, 53, 54] (used to implement DFT in this thesis) implements the projector augmented-wave method (PAW) [55] for treatment of the core regions.

Chapter 3

From energies to measurable properties

Although the use of DFT allows us to determine the electronic ground state energy for the present configuration, a single total energy does not tell us much. In order to draw chemical and physical conclusions about the system, the energies must be related to something.

3.1 Geometry optimization

A calculation performed using DFT generates the energy of the current geometry of a system, and the first thing one is usually interested in, is to find a geometric configuration that reduces the inter-atomic forces in the system, i.e. a local minimum. This geometry can be found by following the energy gradient in every coordinate direction and when the norm of the force components is below a predetermined value, the structure is considered relaxed, and the optimum geometry is found. It is possible to remove some of the degrees of freedom in the system by freezing positions, distances, bonds, or angles in the geometry. This often leads to a faster convergence, but if done carelessly, the procedure may result in an unphysical geometry.

One way of implementing a force minimization is through a steepest decent method (SD) [56]. SD follows the direction in which the forces decrease the fastest, using a set size proportional to the slope of the potential energy surface (PES). Adding a memory of previous search direction to the method results in what is called the conjugate gradient method [57, 58], which is used in this thesis.

As well as E and $\frac{\partial E}{\partial \mathbf{R}}$, the second derivative of the energy $\left(\frac{\partial^2 E}{\partial \mathbf{R}^2}\right)$ can be used for optimizing the structure. When including the Hessian matrix, the optimization is faster thanks to the extended knowledge of the local curvature of the PES. However, the Hessian is, for many systems, prohibitively expensive to calculate and it is, thus, often updated from an initial guess [59].

3.2 AIMD - Ab initio Molecular Dynamics

The PES sampled in the search for low energy structures might contain several local minima, the challenge in this case often turns into finding the local minimum with the lowest energy, i.e. the global minimum. In this search, a method for moving from one local minimum to another is needed. One such method is using the forces obtained from DFT to solve the classical Newtons laws of motion, $F = ma$. To calculate the trajectory in the simulation, the equations of motion are integrated numerically using the Verlet algorithm [60, 61]:

$$R_i(t + \Delta t) \approx 2R_i(t) - R_i(t - \Delta t) + \frac{dv_i(t)}{dt}\Delta t^2. \tag{3.1}$$

This moves the system in time and along the PES. Often, the system is given an initial increase in energy to avoid getting stuck in a local minima.

The two prevailing methods for implementing molecular dynamics in computational code is Born-Oppenheimer Molecular Dynamics (BOMD) [62] (used in this thesis) and Car-Parrinello MD (CPMD)[63]. The first propagates the ionic degrees of freedom by solving the Kohn-Sham equation at each step, the second treats the parameters describing the electronic wave function as classical degrees of freedom and propagates them as such instead of directly solving the wave function at each step.

3.2.1 Controlling the temperature

AIMD simulations are either performed in the canonical (keeping N, V, and T constant) or micro-canonical (keeping N, V, and E constant) ensemble. In this thesis, the canonical ensemble is chosen, and there are several different techniques for controlling the temperature. The majority of these techniques uses an external system, a heat bath, to moderate the temperature; very similarly to how an experimental setup might interact with the surrounding environment. The basic idea of all these methods is to achieve a fixed average temperature, but allowing fluctuations in accordance with a canonical distribution.

Anderson's stochastic collisions

The Anderson thermostat connects the heat bath to the studied system by use of stochastic collisions acting on randomly chosen particles [64]. The new velocities are given by the Maxwell-Boltzmann distribution for the desired temperature. However, the randomness of the assigned velocities may interrupt the dynamics of the system and thus result in a non-physical behaviour.

Berendsen's constant scaling

The Berendsen thermostat [65], which is also called a proportional thermostat, uses velocity scaling of all particles in the system to adjust the temperature. When the

temperature starts to deviate too much from the desired one, all velocities are multiplied by the same factor to move the system dynamics towards the fixed average temperature. This method minimises the local interference of the temperature adjustment. However, the constant scaling of all velocities at once does not always result in a true physical behaviour [66].

Nosé-Hoover's friction moderation

This thesis utilises the Nosé-Hoover [67, 68] thermostat, in which the heat bath is introduced as an additional degree of freedom in the Hamiltonian of the system. The heat bath will work like friction, slowing down och speeding up the particles in the system, such that the electronic response moves the system towards the desired temperature. This method introduces the inherent energy fluctuations of a system with temperature, thus the coupling between the heat bath and the system must be chosen carefully for the process to work. If the coupling is too loose the temperature control will be poor and if it is too tight the system temperature will start to oscillate.

3.3 Transition state search

Moving along the PES and jumping between local minima configurations means crossing an energy barrier as the energy between the sites, by definition, is higher than those of the minima. On a realistic PES, there might be several different paths between two minima. The top of the barrier is a saddle point called a transition state (TS). These saddle points are local maxima only in the direction in which the transition occurs, in all other directions it is a local minimum. To find these reaction paths, methods utilising the first order derivative of the PES are employed. Often it is the reaction path with the lowest TS energy that dominates the kinetics of the system.

The Nudge Elastic Band method (NEB)

As the method name suggests, the idea behind NEB [69, 70] is to attach an elastic band to the initial and final state of the reaction and, tightening the band, forcing it down to the lowest energy path between the states. To determine what this path looks like, intermediate equidistant states are connected with springs along the band and optimised both on spring force and potential energy. The distance between the intermediate states might result in missing the actual position and the exact energy of the saddle point, even though the path is found. An addition to the standard NEB allows the intermediate state closest to the saddle point to climb to the top of the barrier, thereby capturing the energy of the actual transition state [71], as illustrated in fig. 3.1. NEB must be supplied with an initial and a final state. NEB also needs a starting guess of the path, often provided by an interpolation between the two given states [72]. The method will only find the TS closest to the starting guess, i.e. a different starting guess might result in different TS.

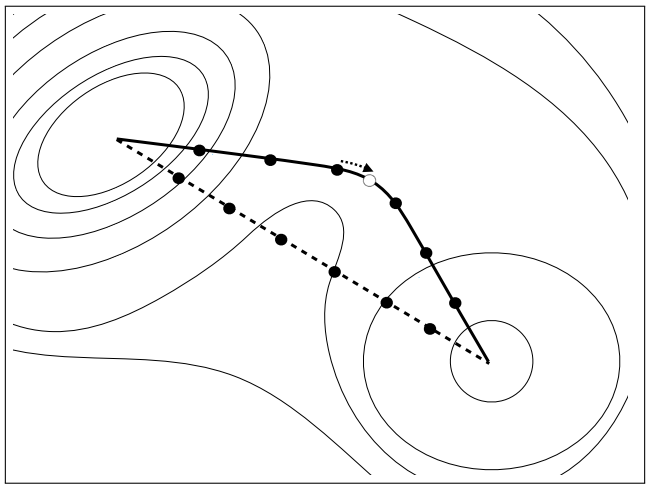

Figure 3.1: The NEB method will use the starting interpolation (dashed line) and find a lower energy path (solid line). When applying the climb option, one image will climb the band, making sure the transition state in captured.

The Dimer method

If the end state of the transition is unknown or for another reason not available, the Dimer method [73] is a transition state tool that only requires an initial state. The Dimer method connects two images by a vector and rotates the second image around the starting guess to find the direction for which the gradient of the vector is the smallest. The procedure is repeated until a first-order saddle point is reached.

These two TS-methods, NEB and Dimer, can be used both individually and concurrently. When calculation the TS in this thesis the NEB with the additional climbing option was chosen.

3.4 Ab initio Thermodynamics

Standard DFT yields the ground-state properties at zero-temperature conditions. In contrast, experiments are performed at elevated temperature and in the presence of reacting gases. To account for a more realistic environment, DFT can be used together with thermodynamics. As compared to MD, ab initio thermodynamics includes temperature and pressure in terms of the free energy change in the system.

3.4.1 Relative stability of different structures

To compare the relative stability of different systems the total energy of the combined systems must be known, along with the energy of the components. Adding atoms to a system means taking them from a reservoir, the cost of taking and moving the atoms can be accounted for in terms of their chemical potential. The standard chemical potential or *standard free energy* [74] is given by,

$$\mu^0(T) = -k_B T \ln \left[\left(\frac{2\pi m k_B T}{h^2} \right)^{3/2} k_B T \right], \tag{3.2}$$

where k_B is Boltzmann's constant, T is the temperature, m is the mass of the atom comprising the gas, and h is Planck's constant. To calculate the maximum of reversible work that can take place in the NVT ensemble under a given set of environmental conditions, the change in Gibbs free energy, ΔG (at a fixed temperature T) is calculated according to

$$\Delta G = \Delta H - T\Delta S, \tag{3.3}$$

where ΔH is the change in enthalpy and ΔS is the change in entropy. When a system reaches equilibrium at constant pressure and temperature, this available free energy, is minimized [75]. When comparing systems where the number of constituents or the included species change, the Gibbs free energy of formation must include the change in chemical potential,

$$\Delta G^{form} = \Delta H - T\Delta S - \Delta\mu. \tag{3.4}$$

In this thesis, the change in enthalpy is approximated as the relative total energy of formation [76], and is given by

$$\Delta H \approx \Delta E^{form} = E_{A+B} - E_A - E_B, \tag{3.5}$$

where E_{A+B} is the energy of the total system, E_{rA} the energy of system A, and E_B the energy of system B. ΔS in eq. (3.4) is the difference in entropy between system $A + B$ and system A,

$$\Delta S = S_{A+B} - S_A, \tag{3.6}$$

while the entropy of system B, the chemical potential, is calculated calculated in relation to a chosen reference pressure

$$\Delta\mu(T, p) = \mu^o(T, p^o) + k_B T \ln \left(\frac{p}{p_o} \right). \tag{3.7}$$

To calculate the entropies in eq. (3.6), the partition function of the systems must be known and, thus, the vibrational frequencies of the relevant species calculated. In this thesis, the translational degrees of freedom were calculated using the ideal gas-approximation whereas their vibrations, along with the vibrations of the zeolite systems, were approximated as harmonic oscillators as per the implementation in the Atomic Simulation Environment (ASE) [77, 78].

3.4.2 Molecular vibrations

A non-linear molecule of N atoms has 3N degrees of freedom corresponding to translations, rotations, and vibrations. 3N-6 of these are normal modes of vibration, the 6 degrees of freedom removed being those of translation and rotation in 3 dimensions (a linear molecule has 3N-5 degrees of freedom since rotation along the axis of the molecule has an infinite symmetry number). The vibrations are oscillations around the equilibrium structure found by a geometry optimization. The composition and character of the bonds determine the vibrational frequencies, which becomes an identifying characteristic of the molecule.

When calculating the vibrational frequencies, all degrees of freedom related to movements in space (i.e. translations and rotations) will be (close to) zero, only the true vibrational degrees of freedom will have positive values. For a transition state, the configuration is not at a local minima, and is thus possible to displace along the reaction path. Depending on the shape of the TS, one or more of the vibrational degrees of freedom will then be characterized by imaginary frequencies.

3.5 Reaction kinetics

One of the purposes of using a catalyst is to divert a reaction into a new, more energetically favorable path, thereby increasing the rate of the reaction. This new catalyzed reaction path is identified using the tools introduced previously in this chapter, resulting in a reaction mechanism with the characteristics of that in fig. 1.1. Connecting the identified reaction to experimentally measurable conversion and selectivity, can be done through kinetic modeling. The first step in kinetic modeling is to calculate the rate of the reaction.

3.5.1 Time evolution of the reaction

To get the time evolution of the system, a master equation [79] is used. In this context, all reaction intermediates and TSs are referred to as *states*, and the master equation describes the changing probability of finding the system in a given state. Written in the form

$$\frac{d\mathcal{P}_\alpha}{dt} = \sum_\beta \left(W_{\beta\alpha}\mathcal{P}_\alpha - W_{\alpha\beta}\mathcal{P}_\beta \right), \tag{3.8}$$

the equation gives the change in probability of finding the system in state α, where $W_{\beta\alpha}$ is the transition rate from state β to state α and $\mathcal{P}_\alpha$ is the probability of finding the system in state α. The sum over β account for all paths to α.

Mean-field approximation

In a system of single-site catalysts, the distance between the active sites implies no interaction between different sites and for a sufficiently large number of sites, a mean-

field approximation [7] (additionally assuming an even and random distribution of the reactants) should be acceptable. With this approximation, the probability of being in state α is the average concentration of α.

Transition State Theory (TST)

To calculate the rate for a transition, i.e. $W_{\beta\alpha}$ or $W_{\alpha\beta}$ in eq. (3.8), rate constants are estimated using transition state theory (TST) [80]. Moving from the reactant R, through the activated transition state $R^{\ddagger}$ to the product state P, can be visualized as

$$R \rightleftharpoons R^{\ddagger} \rightarrow P. \tag{3.9}$$

In TST, recrossing the barrier is not allowed, hence the one way arrow between $R^{\ddagger}$ and P. However, the back reaction is gained from letting R and P switch places. From this, the rate at which a given reaction occurs is given by the probability of being in the TS compared to that of being in the reactant state, times the *trial frequency* f,

$$W_{\beta\alpha} = f\frac{\mathcal{P}(R^{\ddagger})}{\mathcal{P}(R)} = f\frac{Z^{\ddagger}}{Z}. \tag{3.10}$$

The trial frequency is generally considered to be the vibration along the reaction coordinate, i.e. the vibration crossing the TS. The second identity in eq. (3.10) comes from the mean field approximation, equating the probability of being in a state with the partition function of that particular state. Assuming that the system follows the Boltzmann distribution and that the trial frequency is low ($k_B T >> hf$), and relating the energy of the TS to that of the reactant, the rate becomes

$$W_{\beta\alpha} = \frac{k_B T}{h}\frac{Z'^{\ddagger}}{Z}e^{\frac{-\Delta E}{k_B T}} = k_{TST}, \tag{3.11}$$

where ΔE is the energy difference between the two states, and $Z'^{\ddagger}$ and Z are the partition functions with reference to the local energy minima. The reaction coordinate has been excluded in $Z'^{\ddagger}$. k_{TST} is the transition state rate constant.

In steady-state, the time derivative of the rate in eq. (3.8) equals zero. For a closed system, this implies an equilibrium between the reactants and the product.

Chapter 4

Cu-SSZ-13 during methane-to-methanol direct conversion

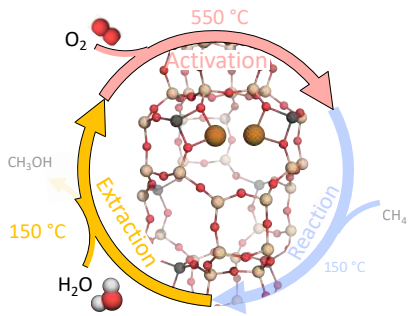

(a) Paper I: The stability of different Cu_2-cluster structures are investigated in the context of direct methane-to-methanol conversion.

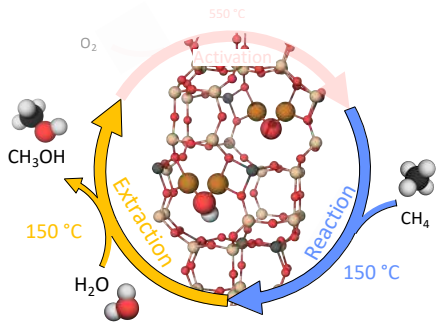

(b) Paper II: The reaction mechanism is investigated over the most stable active site motifs.

Figure 4.1: The two papers included in this thesis investigate the structure of the active site during the conditions of reaction, and what path the reaction would take over the identified site motifs.

Studies of the 4/5/6/10 MR MFI zeolite ZSM-5 has shown catalytic activity for the direct conversion of methane to methanol, with the cation system of Cu-ZSM-5 being the most active for the conversion [81], although the detailed configuration of the active site is still under debate [82, 83, 84]. In addition to methane conversion, the Cu-ZMS-5 structure has also shown the ability to promote the selective catalytic reduction of NO_x using NH_3 as reducing agent [85]. However, ZSM-5 is in this process out-preformed by the small-pored chabazite (CHA) system of Cu-SSZ-13 [86]. A natural next step would be to investigate whether the small pore zeolite system would act as a catalyst for the direct methane-to-methanol reaction as well. The experimental reaction cycle for partial oxidation of methane to methanol over zeolites is a quasi-catalytic three step process: activation of the oxidant (O_2, N_2O, or NO) at high temperature (>350°C); reaction phase at 50-210°C and addition of CH_4; extraction at 25-210°C where reactants are flushed out using water/ethanol or an other solvent [17, 87]. To design a functional catalyst we would

like to know what the material looks like during reaction conditions, as well as how the reaction proceeds over the active sites of the catalytic material.

The SSZ-13 was modeled using the small unit sell of 12 T-sites and an Si:Al ratio of 10:2. The position of the aluminum atoms were chosen as the most energetically favorable positions while also adhearing to Löwenstein's rule, stating that two AlO_4-tetrahedrons are not allowed to share an oxygen bond [88]. To compensate for the introduced charge, one copper for each aluminum was added to the system. Thus, this $Z_2[Cu_2]$ motif formed the initial configuration of the active site. The notation Z_2 is here chosen to emphasize the Si:Al=10:2 ratio in the SSZ-13 framework.

The first topic of investigation is to determine how the experimental conditions of the activation and extraction phase affects the $Z_2[Cu_2]$ motif (see fig. 4.1aa)). The stability of different $Cu_2O_xH_y$ clusters in the zeolite were, thus, compared.

When the most stable motifs of the active site were identified, the partial oxidation of methane was performed over the systems. The conditions of reaction and extraction was applied, as seen in fig. 4.1b. Both active site motifs were investigated separately and the reaction landscape elucidated. In addition, as the zeolite was found to be very humid, the effects of water on the reaction landscape was also investigated. Finally, to relate the reaction mechanism to experimental findings, a micro-kinetic model was made for each motif.

4.1 Paper I: Cu-dimer active site motifs during reaction conditions

In the phase diagram of fig. 4.2, the stable cluster structures are shown for a range of conditions. It is found that the stable state is dependent on temperature and pressure, as well as the starting configuration of the cluster. A cluster formed from the already oxidized Cu_2O will in general be more stable than one formed from Cu_2. The Cu_2O structure also stabilizes larger clusters. At lower temperature and higher partial pressure of oxygen, the zeolite is very humid, thus both adsorbed and free water molecules are present when temperature decreases. However, for experimentally relevant temperatures and pressures, only the Cu_2O and the Cu_2OH are thermodynamically feasible active site configurations.

With the two most stable active site motives identified, the reaction mechanism over the two sites was investigated in paper II.

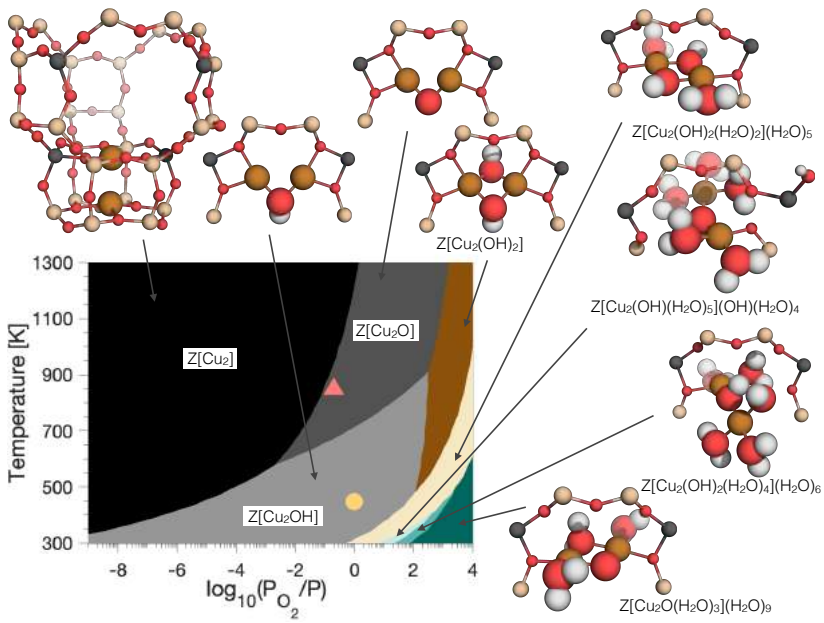

Figure 4.2: Phase diagram of oxidized Cu_2-clusters in SSZ-13. At higher temperature and lower partial pressure (top left corner), the Cu_2 situated inside the double 6MR is the most stable configuration. Decreasing temperature and increasing the partial pressure of O_2 means moving first to Cu_2O and then Cu_2OH and $Cu_2(OH)_2$ clusters. At lower temperature and higher pressures the cage becomes very humid. The red triangle (848 K, 20% oxygen, 10^{-8}% water) corresponds to activation conditions, and the yellow circle (448 K, 4% water, 10^{-8}% oxygen) corresponds to the conditions of extraction [87].

4.2 Paper II: Reaction mechanism over Cu_2O and Cu_2OH

The reaction (over both sites) start with the activation of the C-H bond in CH_4 through a methyl radical, CH_3*. This TS is responsible for the highest barrier in the path, 0.99 eV and 2.91 eV, for the $Z_2[Cu_2O]$ and $Z_2[Cu_2OH]$ site, respectively. In both systems, the reaction path under dry conditions (T=448 K and $p_{CH_4} = 2\%$, $p_{H_2O} = 10\%$, and $p_{CH_3OH} = 10^{-9}\%$, with respect to atmospheric pressure) is endergonic. The reaction over $Z_2[Cu_2O]$ passes through two intermediate states (see fig. 4.3). Depending on how much water is added to the reaction, the reaction may have three possible final structures. The final desorption of methanol under dry conditions is at a cost of 0.72 eV, while the path including one water are exergonic at -0.39 eV. The need for a solvent in the quasi-catalytic reaction [17] is, thus, confirmed on this particular active site.

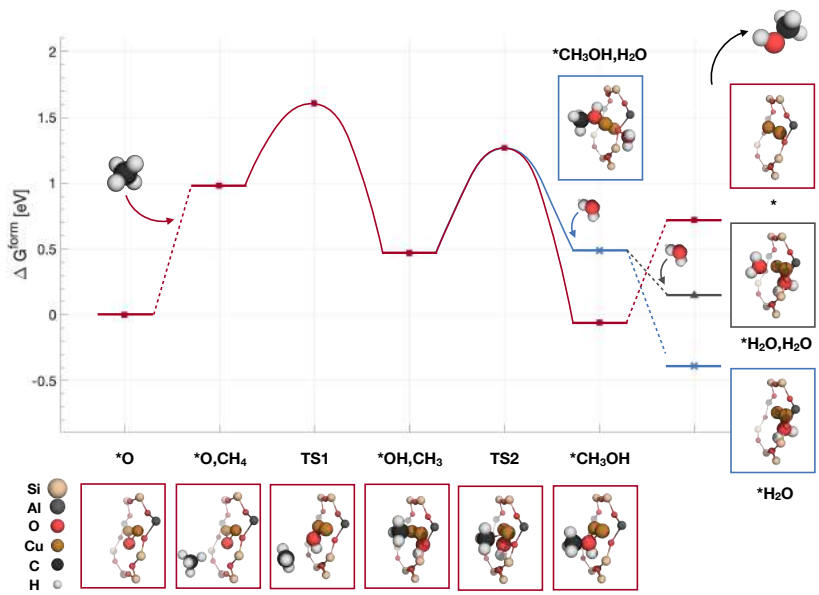

Figure 4.3: Reaction path over $Z_2[Cu_2O]$ in SSZ-13. Without water in the reaction, the reaction is endergonic. The red squared path shown the reaction during dry conditions, and is endergonic. Adding water to the mechanism gives the blue cross path for one H_2O, and the gray triangle path for two H_2O. For these two reaction paths the energy of the final desorption of CH_3OH is lowered, producing an exergonic reaction path. Reaction conditions are set to T=448 K, $p_{CH_4} = 2\%$, $p_{H_2O} = 10\%$, and $p_{CH_3OH} = 10^{-9}\%$, with respect to atmospheric pressure.

Over the $Z_2[Cu_2OH]$ site, there are two different possible intermediates in the first reaction step. One forming a bound CH_3OH molecule directly on the active site, the other passing through a surface stabilized CH_3, which requires adding water for the reaction to proceed and produce methanol in the next step. However, according to fig. 4.4, none of the

mechanisms will take place over the $Z_2[Cu_2OH]$ motif. Both with and without water in the reaction, the explored paths are endergonic. The desorption of methanol has the lowest cost under dry conditions, at 1.53 eV, contradicting the use of a solvent to extract methanol. Even though the desorption step itself is exergonic at -0.51 eV, the complete reaction is performed at a minimum cost of 1.53 eV. Adding one and two water molecules increases the desorption energies to -0.31 eV and 1.13 eV, or an overall cost of 2.00 eV and 3.76 eV, respectively.

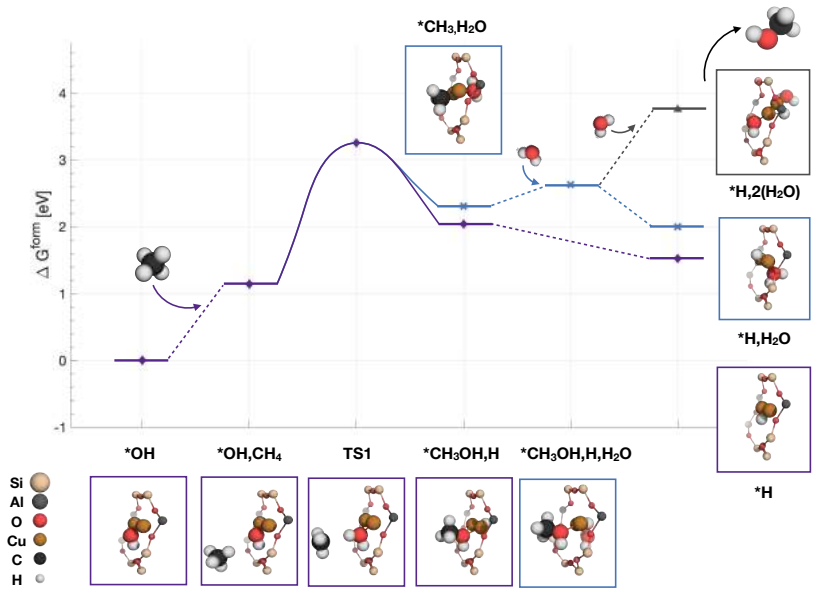

Figure 4.4: Reaction path over $Z_2[Cu_2OH]$ in SSZ-13. Purple diamonds mark the mechanism under dry conditions, blue cross the addition of one H_2O, and gray triangles when two H_2O are included in the reaction. All explored paths are endergonic. Over $Z_2[Cu_2OH]$, the reaction under dry conditions has the lowers energy cost. The inclusion of water into the mechanism increases the free energy of the system and thus the desorption energy for methanol. Reaction conditions are set to T=448 K, $p_{CH_4} = 2\%$, $p_{H_2O} = 10\%$, and $p_{CH_3OH} = 10^{-9}\%$, with respect to atmospheric pressure.

Micro-kinetic model

With the help of a micro-kinetic model, using the reaction paths shown in figs. 4.3 and 4.4, the performance of the active site, e.g. over time, can be analyzed. In fig. 4.5 the activity of the site is shown as the active site half-time, i.e. how fast half of the active sites in a system has undergone a full reaction, as a function of temperature. It has been shown that ZSM-5 can facilitate partial oxidation of methane and the $Z_2[Cu_2O]$ is one

of the structures proposed as the active site [82, 81], and in fig. 4.5 the $Z_2[Cu_2O]$ and $Z_2[Cu_2OH]$ sites in SSZ-13 are compared to the same reaction mechanism performed over the $Z_2[Cu_2O]$ site in the large pore zeolite ZSM-5 [81].

Table 4.1: The elementary reactions used in the micro-kinetic model of the reaction over the sites in Cu-SSZ-13. The notation is *X,Y, with X forming the current state of the active site, and Y as either adsorbed on the active site or free in the zeolite cage.

Site	Reaction			Type
$Z_2[Cu_2O]$	$*O + CH_4(g)$	$\rightleftharpoons$	$*O,CH_4$	adsorption
	$*O,CH_4$	$\rightleftharpoons$	$*OH,CH_3$	surface reaction
	$*OH,CH_3$	$\rightleftharpoons$	$*CH_3OH$	surface reaction
	$*CH_3OH$	$\rightleftharpoons$	$* + CH_3OH(g)$	desorption
$Z_2[Cu_2OH]$	$*OH + CH_4(g)$	$\rightleftharpoons$	*OH,CH4	adsorption
	$*OH,CH_4$	$\rightleftharpoons$	$*H,CH_3OH$	surface reaction
	$*H,CH_3OH$	$\rightleftharpoons$	$*H + CH_3OH(g)$	desorption

In the description of intermediate steps in the reaction mechanism, the two copper atoms of the active site is denoted by *. A structure denoted *X,Y implies that reaction intermediate X is coordinated to both Cu atoms, forming the current state of the active site, while reaction intermediate Y is either adsorbed in the active site or free in the zeolite cage; all reaction steps under dry conditions are described in table 4.1, for $Z_2[Cu_2O]$ and $Z_2[Cu_2O]$, respectively.

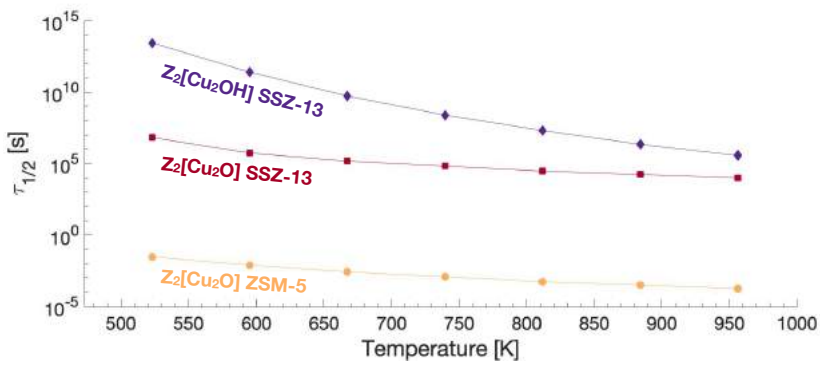

Figure 4.5: The active site half-time as a function of temperature. The $Z_2[Cu_2O]$ and $Z_2[Cu_2OH]$ sites are here compared to that of the same reaction performed over the $Z_2[Cu_2O]$ site in the large pore zeolite ZSM-5 [81].

The micro-kinetic model follows the result of the free energies in fig. 4.4, clearly showing that neither of the sites in SSZ-13 are good candidates for methane-to-methanol conversion. With a half-time of $10^{13} - 10^{3}$s, neither the $Z_2[Cu_2O]$ nor $Z_2[Cu_2OH]$ motifs, are likely responsible for any activity in the material. For the temperature range shown, the $Z_2[Cu_2O]$ MFI structure is the most active site. This corresponds well with experiments where large pore zeolites (such as ZSM-5 or mordenite) has a larger turnover than small pore zeolite (such as SSZ-13) [89].

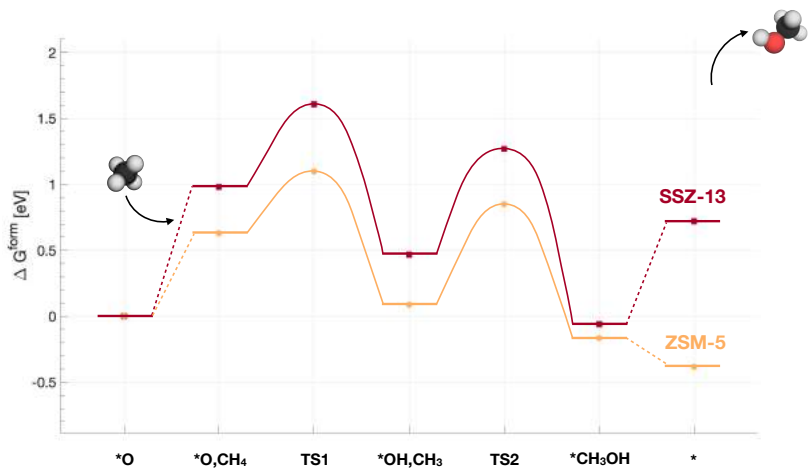

Figure 4.6: Reactions path over $Z_2[Cu_2O]$ in SSZ-13 (red squares), and ZMS-5 (yellow dots). The difference in activity for the reaction can be traced to the first TS, that of the methyl radical, and the energy of desorption of the CH_3OH molecule, which is exergonic only for the ZSM-5 system. Reaction conditions are set to T=448 K, $p_{CH_4} = 2\%$, and $p_{CH_3OH} = 10^{-9}\%$, with respect to atmospheric pressure.

Comparing the Gibbs free energies landscapes of the $Z_2[Cu_2O]$ in SSZ-13 (red squares), and ZMS-5 (yellow dots) in fig. 4.6, makes it possible to trace the cause of the difference in activity between the two systems. The ZSM-5 is consistently lower in free energy. The highest barrier in both systems is the first TS, corresponding to the methyl radical. In SSZ-13 it is calculated to 1.60 eV, as compared to 1.10 eV in ZSM-5. The second barrier is 0.80 eV in SSZ-13 and 0.76 eV. Thus, the 0.50 eV higher barrier to break the first C-H bond explains the lower activity of the $Z_2[Cu_2O]$ site in SSZ-13. One further limit to the activity is posed by the desorption of methanol. The desorption in SSZ-13 is at a cost of 0.78 eV, while it is an exergonic step of -0.22 eV in ZSM-5. Under dry conditions, it is exergonic to desorb methanol only in the ZMS-5 system.

Chapter 5

Conclusions and Outlook

In Paper I and II, the stability and activity of Cu-SSZ-13 has been investigated for direct methane-to-methanol conversion using ab initio thermodynamics and micro-kinetic modeling. The structure of the active site in the zeolite is found to be highly dependent on temperature and pressure. At low temperature conditions, a plethora of active site motifs are energetically feasible, and the system is likely to be very humid. This is in good correspondence with what has been known about zeolite since their discovery [90]. However, increasing the temperature makes the water leave the system, thereby reducing the number of motifs to two, namely the $Z_2[Cu_2O]$ and $Z_2[Cu_2OH]$ structures. The inherent humidity of the system turn out to be an important factor for whether the conversion is thermodynamically feasible or not. The presence of water has a most pronounced effect as it enables desorption of methanol. However, in both dry and humid conditions, the activity of the investigated active site motifs is low, much lower than that of ZSM-5. This discrepancy between stability and activity, as clearly presented by the inactivity of the Cu-SSZ-13 sites, highlights a very important fact: the most stable, and thus prevalent structure is not necessarily the one responsible for the activity.

It should be noted that in the experimental procedure used as a reference for the applied conditions, the temperature is adjusted to reactivate the active sites. This makes it only a quasi-catalytic process. Thus, the same is true for the investigated reaction path where neither the initial activation nor the subsequent reactivation of the active site is accounted for. A future challenge will be to close the cycle and make it into a truly catalytic process.

Chapter 6

Acknowledgement

The research work in this thesis has been carried out at the Division of Chemical Physics at the Department of Physics and the Competence Center for Catalysis (KCK) at Chalmers University of Technology, Sweden.

This research is financially supported by the Knut och Alice Wallenberg fundation. The Competence Center for Catalysis is financially supported by Chalmers University of Technology, the Swedish Energy Agency and the member companies: AB Volvo, ECAPS AB, Johnson Matthey AB, Preem AB, Scania CV AB, Umicore Denmark ApS and Volvo Car Corporation AB. The calculations have been performed at C3SE (Göteborg) through a SNIC grant.

I would like to thank:
My main supervisor, Anders Hellman. My co-supervisor, Henrik Grönbeck. All my colleagues at Chemical Physics, as well as the members of KCK and the KAW-group. Last but not least I would also like to thank my family.

References

[1] U.S. Energy Information Administration (EIA). *International Energy Outlook 2019*. Sept. 2019.

[2] B. Afework et al. *Hydrocarbon Combustion*. Accessed October 31, 2019.

[3] *Methane*. Accessed October 31, 2019.

[4] C. N. Satterfield. *Heterogeneous Catalysis in Industrial Practice*. Krieger Publishing Company, 1996. ISBN: 9781575240022.

[5] T. Letcher. *Future Energy: Improved, Sustainable and Clean Options for our Planet*. Elsevier Science, 2008. ISBN: 9780080564876.

[6] P. Sabatier. Hydrogénations et déshydrogénations par catalyse. *Berichte der deutschen chemischen Gesellschaft* **44**.3 (1911), 1984–2001. DOI: 10.1002/cber.19110440303.

[7] I. Chorkendorff and J. Niemantsverdriet. *Concepts of Modern Catalysis and Kinetics*. Wiley, 2006. ISBN: 9783527605644.

[8] J. M. Thomas, R. Raja, and D. W. Lewis. Single-Site Heterogeneous Catalysts. *Angewandte Chemie International Edition* **44**.40 (2005), 6456–6482. DOI: 10.1002/anie.200462473.

[9] S. Sirajuddin and A. C. Rosenzweig. Enzymatic Oxidation of Methane. *Biochemistry* **54**.14 (Apr. 2015), 2283–2294. DOI: 10.1021/acs.biochem.5b00198.

[10] A. Rosenzweig, C. Frederick, and S. e. a. Lippard. Crystal structure of a bacterial non-haem iron hydroxylase that catalyses the biological oxidation of methane. *Nature* 366 (Dec. 1993), 537–543. DOI: doi.org/10.1038/366537a0.

[11] N. A. Elango et al. Crystal structure of the hydroxylase component of methane monooxygenase from Methylosinus trichosporium OB3b. *Protein Science* **6**.3 (1997), 556–568. DOI: 10.1002/pro.5560060305.

[12] *Database of zeolite structures*. 2017. URL: http://www.iza-structure.org/databases/.

[13] F. Göltl and J. Hafner. Structure and properties of metal-exchanged zeolites studied using gradient-corrected and hybrid functionals. I. Structure and energetics. *The Journal of Chemical Physics* **136**.6 (2012), 064501. DOI: 10.1063/1.3676408.

[14] E. V. Starokon et al. Room-Temperature Oxidation of Methane by -Oxygen and Extraction of Products from the FeZSM-5 Surface. *The Journal of Physical Chemistry C* **115**.5 (2011), 2155–2161. DOI: 10.1021/jp109906j.

[15] S. E. Bozbag et al. Methane to methanol over copper mordenite: yield improvement through multiple cycles and different synthesis techniques. *Catal. Sci. Technol.* **6** (13 2016), 5011–5022. DOI: 10.1039/C6CY00041J.

[16] M. J. Wulfers et al. Conversion of methane to methanol on copper-containing small-pore zeolites and zeotypes. *Chem. Commun.* **51** (21 2015), 4447–4450. DOI: 10.1039/C4CC09645B.

[17] M. H. Groothaert et al. Selective Oxidation of Methane by the Bis(μ-oxo)dicopper Core Stabilized on ZSM-5 and Mordenite Zeolites. *Journal of the American Chemical Society* **127**.5 (2005), 1394–1395. DOI: 10.1021/ja047158u.

[18] J. Thijssen. *Computational Physics*. 2nd ed. Cambridge University Press, 2007. DOI: 10.1017/CBO9781139171397.

[19] M. Born and R. Oppenheimer. Zur Quantentheorie der Molekeln. *Annalen der Physik* **389**.20 (1927), 457–484. DOI: 10.1002/andp.19273892002.

[20] D. R. Hartree. The Wave Mechanics of an Atom with a Non-Coulomb Central Field. Part I. Theory and Methods. *Mathematical Proceedings of the Cambridge Philosophical Society* **24**.1 (1928), 89–110. DOI: 10.1017/S0305004100011919.

[21] V. Fock. Näherungsmethode zur Lösung des quantenmechanischen Mehrkörperproblems. *Zeitschrift für Physik* **61**.1 (Jan. 1930), 126–148. ISSN: 0044-3328. DOI: 10.1007/BF01340294.

[22] D. R. Hartree and W. Hartree. Self-Consistent Field, with Exchange, for Beryllium. *Proceedings of the Royal Society of London Series A* **150**.869 (May 1935), 9–33. DOI: 10.1098/rspa.1935.0085.

[23] J. C. Slater. The Theory of Complex Spectra. *Phys. Rev.* **34** (10 Nov. 1929), 1293–1322. DOI: 10.1103/PhysRev.34.1293.

[24] P. Hohenberg and W. Kohn. Inhomogeneous Electron Gas. *Phys. Rev.* **136** (3B Nov. 1964), B864–B871. DOI: 10.1103/PhysRev.136.B864.

[25] J. Sakurai and J. Napolitano. *Modern Quantum Mechanics*. Addison-Wesley, 2011. ISBN: 9780321503367.

[26] J. Kohanoff. *Electronic Structure Calculations for Solids and Molecules: Theory and Computational Methods*. Cambridge University Press, 2006. DOI: 10.1017/CBO9780511755613.

[27] W. Kohn and L. J. Sham. Self-Consistent Equations Including Exchange and Correlation Effects. *Phys. Rev.* **140** (4A Nov. 1965), A1133–A1138. DOI: 10.1103/PhysRev.140.A1133.

[28] G. L. Oliver and J. P. Perdew. Spin-density gradient expansion for the kinetic energy. *Phys. Rev. A* **20** (2 Aug. 1979), 397–403. DOI: 10.1103/PhysRevA.20.397.

[29] O. Gunnarsson and B. I. Lundqvist. Exchange and correlation in atoms, molecules, and solids by the spin-density-functional formalism. *Phys. Rev. B* **13** (10 May 1976), 4274–4298. DOI: 10.1103/PhysRevB.13.4274.

[30] J. Sun et al. Self-consistent meta-generalized gradient approximation within the projector-augmented-wave method. *Phys. Rev. B* **84** (3 July 2011), 035117. DOI: 10.1103/PhysRevB.84.035117.

[31] L. Chen et al. Mechanism for Solid-State Ion Exchange of Cu+ into Zeolites. *The Journal of Physical Chemistry C* **120**.51 (2016), 29182–29189. DOI: 10.1021/acs.jpcc.6b09553.

[32] J. P. Perdew et al. Atoms, molecules, solids, and surfaces: Applications of the generalized gradient approximation for exchange and correlation. *Phys. Rev. B* **46** (11 Sept. 1992), 6671–6687. DOI: 10.1103/PhysRevB.46.6671.

[33] D. C. Langreth and M. J. Mehl. Beyond the local-density approximation in calculations of ground-state electronic properties. *Phys. Rev. B* **28** (4 Aug. 1983), 1809–1834. DOI: 10.1103/PhysRevB.28.1809.

[34] A. D. Becke. Density-functional thermochemistry. III. The role of exact exchange. *The Journal of Chemical Physics* **98**.7 (1993), 5648–5652. DOI: 10.1063/1.464913.

[35] J. Heyd, G. E. Scuseria, and M. Ernzerhof. Hybrid functionals based on a screened Coulomb potential. *The Journal of Chemical Physics* **118**.18 (2003), 8207–8215. DOI: 10.1063/1.1564060.

[36] S. Grimme. Accurate description of van der Waals complexes by density functional theory including empirical corrections. *Journal of Computational Chemistry* **25**.12 (2004), 1463–1473. DOI: 10.1002/jcc.20078.

[37] S. Grimme. Semiempirical GGA-type density functional constructed with a long-range dispersion correction. *Journal of Computational Chemistry* **27**.15 (2006), 1787–1799. DOI: 10.1002/jcc.20495.

[38] S. Grimme et al. A consistent and accurate ab initio parametrization of density functional dispersion correction (DFT-D) for the 94 elements H-Pu. *The Journal of Chemical Physics* **132**.15 (2010), 154104. DOI: 10.1063/1.3382344.

[39] A. D. Becke and E. R. Johnson. Exchange-hole dipole moment and the dispersion interaction. *The Journal of Chemical Physics* **122**.15 (2005), 154104. DOI: 10.1063/1.1884601.

[40] B. I. Lundqvist et al. Density functional theory including Van Der Waals forces. *International Journal of Quantum Chemistry* **56**.4 (1995), 247–255. DOI: 10.1002/qua.560560410.

[41] M. Levy and S. Vuckovic. *The Adiabatic Connection Formula for the Exchange–Correlation Functional*. 2017.

[42] M. Dion et al. Van der Waals Density Functional for General Geometries. *Phys. Rev. Lett.* **92** (24 June 2004), 246401. DOI: 10.1103/PhysRevLett.92.246401.

[43] K. Lee et al. Higher-accuracy van der Waals density functional. *Phys. Rev. B* **82** (8 Aug. 2010), 081101. DOI: 10.1103/PhysRevB.82.081101.

[44] K. Berland and P. Hyldgaard. Exchange functional that tests the robustness of the plasmon description of the Van der Waals density functional. *Phys. Rev. B* **89**.3 (2014), 035412.

[45] A. H. Larsen et al. Localized atomic basis set in the projector augmented wave method. *Phys. Rev. B* **80** (19 Nov. 2009), 195112. DOI: 10.1103/PhysRevB.80.195112.

[46] P. Schwerdtfeger. The Pseudopotential Approximation in Electronic Structure Theory. *ChemPhysChem* **12**.17 (2011), 3143–3155. DOI: 10.1002/cphc.201100387.

[47] E. S. Sachs, J. Hinze, and N. H. Sabelli. Frozen core approximation, a pseudopotential method tested on six states of NaH. *The Journal of Chemical Physics* **62**.9 (1975), 3393–3398. DOI: 10.1063/1.430993.

[48] G. Kresse and J. Hafner. Ab Initio molecular dynamics for liquid metals. *Phys. Rev. B* **47**.1 (1993), 558–561. DOI: 10.1103/PhysRevB.47.558.

[49] G. Kresse and J. Furthmüller. Efficiency of Ab-Initio Total Energy Calculations for Metals and Semiconductors Using a Plane-Wave Basis Set. *Computational Materials Science* **6**.1 (1996), 15–50. ISSN: 0927-0256. DOI: 10.1016/0927-0256(96)00008-0.

[50] G. Kresse and J. Furthmüller. Efficient Iterative Schemes for Ab Initio Total-Energy Calculations Using a Plane-Wave Basis Set. *Phys. Rev. B* **54**.16 (1996), 11169–11186. DOI: 10.1103/PhysRevB.54.11169.

[51] G. Kresse and J. Hafner. Norm-conserving and ultrasoft pseudopotentials for first-row and transition elements. *Journal of Physics Condensed Matter* **6** (1994), 8245–8257. DOI: 10.1088/0953-8984/6/40/015.

[52] G. Kresse and D. Joubert. From ultrasoft pseudopotentials to the projector augmented-wave method. *Phys. Rev. B* **59** (3 1999), 1758–1775. DOI: 10.1103/PhysRevB.59.1758.

[53] J. Klimeš, D. R Bowler, and A. Michaelides. Chemical accuracy for the Van der Waals density functional. *Journal of physics. Condensed matter* **22** (2010), 022201. DOI: 10.1088/0953-8984/22/2/022201.

[54] J. Klimeš, D. R. Bowler, and A. Michaelides. Van der Waals density functionals applied to solids. *Phys. Rev. B* **83** (19 2011), 195131. DOI: 10.1103/PhysRevB.83.195131.

[55] P. E. Blöchl. Projector augmented-wave method. *Phys. Rev. B* **50** (24 Dec. 1994), 17953–17979. DOI: 10.1103/PhysRevB.50.17953.

[56] P. Debye. Näherungsformeln für die Zylinderfunktionen für große Werte des Arguments und unbeschränkt veränderliche Werte des Index. *Mathematische Annalen* **67**.4 (Dec. 1909), 535–558. ISSN: 1432-1807. DOI: 10.1007/BF01450097.

[57] M. R. Hestenes and E. L. Stiefel. Methods of Conjugate Gradients for Solving Linear Systems. *Journal of Research of the National Bureau of Standards* **49** (6 Dec. 1952), 409–436. DOI: 10.6028/jres.049.044.

[58] S. T. W.H. Press B.P. Flannery and W. Vetterling. *Numerical Recipes*. Cambridge University Press, 1986.

[59] J. D. Head and M. C. Zerner. A Broyden-Fletcher-Goldfarb-Shanno optimization procedure for molecular geometries. *Chemical Physics Letters* **122**.3 (1985), 264–270. ISSN: 0009-2614. DOI: doi.org/10.1016/0009-2614(85)80574-1.

[60] L. Verlet. Computer "Experiments" on Classical Fluids. I. Thermodynamical Properties of Lennard-Jones Molecules. *Phys. Rev.* **159** (1 July 1967), 98–103. DOI: 10.1103/PhysRev.159.98.

[61] W. C. Swope et al. A computer simulation method for the calculation of equilibrium constants for the formation of physical clusters of molecules: Application to small water clusters. *The Journal of Chemical Physics* **76**.1 (1982), 637–649. DOI: 10.1063/1.442716.

[62] R. Barnett et al. Born-Oppenheimer dynamics using density-functional theory: Equilibrium and fragmentation of small sodium clusters. *Chemical Physics - CHEM PHYS* **94** (Jan. 1991), 608–616. DOI: 10.1063/1.460327.

[63] R. Car and M. Parrinello. Unified Approach for Molecular Dynamics and Density-Functional Theory. *Phys. Rev. Lett.* **55** (22 Nov. 1985), 2471–2474. DOI: 10.1103/PhysRevLett.55.2471.

[64] H. C. Andersen. Molecular dynamics simulations at constant pressure and/or temperature. *The Journal of Chemical Physics* **72**.4 (1980), 2384–2393. DOI: 10.1063/1.439486.

[65] H. J. C. Berendsen et al. Molecular dynamics with coupling to an external bath. *The Journal of Chemical Physics* **81**.8 (1984), 3684–3690. DOI: 10.1063/1.448118.

[66] S. C. Harvey, R. K.-Z. Tan, and T. E. Cheatham III. The flying ice cube: Velocity rescaling in molecular dynamics leads to violation of energy equipartition. *Journal of Computational Chemistry* **19**.7 (1998), 726–740.

[67] S. Nosé. A unified formulation of the constant temperature molecular dynamics methods. *The Journal of Chemical Physics* **81**.1 (1984), 511–519. DOI: 10.1063/1.447334.

[68] W. G. Hoover. Canonical dynamics: Equilibrium phase-space distributions. *Phys. Rev. A* **31** (3 Mar. 1985), 1695–1697. DOI: 10.1103/PhysRevA.31.1695.

[69] D. Sheppard, R. Terrell, and G. Henkelman. Optimization methods for finding minimum energy paths. *The Journal of Chemical Physics* **128**.13 (2008), 134106. DOI: 10.1063/1.2841941.

[70] G. Henkelman and H. Jónsson. Improved tangent estimate in the nudged elastic band method for finding minimum energy paths and saddle points. *The Journal of Chemical Physics* **113**.22 (2000), 9978–9985. DOI: 10.1063/1.1323224.

[71] G. Henkelman, B. P. Uberuaga, and H. JÃ³nsson. A climbing image nudged elastic band method for finding saddle points and minimum energy paths. *The Journal of Chemical Physics* **113**.22 (2000), 9901–9904. DOI: 10.1063/1.1329672.

[72] S. Smidstrup et al. Improved initial guess for minimum energy path calculations. *The Journal of Chemical Physics* **140**.21 (2014), 214106. DOI: 10.1063/1.4878664.

[73] G. Henkelman and H. Jónsson. A dimer method for finding saddle points on high dimensional potential surfaces using only first derivatives. *The Journal of Chemical Physics* **111**.15 (1999), 7010–7022. DOI: 10.1063/1.480097.

[74] T. Hill. *An Introduction to Statistical Thermodynamics*. Addison-Wesley series in chemistry. Dover Publications, 1986. ISBN: 9780486652429.

[75] J. Gibbs. A Method of Geometrical Representation of the Thermodynamic Properties of Substances by Means of Surfaces. *Transactions of the Connecticut Academy of Arts and Sciences* **2** (1873), 382–404.

[76] K. Reuter and M. Scheffler. Composition, structure, and stability of RuO_2(110) as a function of oxygen pressure. *Phys. Rev. B* **65** (Jan. 2001), 1–11.

[77] A. H. Larsen et al. The atomic simulation environment—a Python library for working with atoms. *Journal of Physics: Condensed Matter* **29**.27 (2017), 273002.

[78] S. R. Bahn and K. W. Jacobsen. An object-oriented scripting interface to a legacy electronic structure code. English. **4**.3 (2002), 56–66. ISSN: 1521-9615. DOI: 10.1109/5992.998641.

[79] A. Jansen. *An Introduction to Kinetic Monte Carlo Simulations of Surface Reactions*. Lecture Notes in Physics. Springer Berlin Heidelberg, 2010. ISBN: 9783642294884.

[80] H. Eyring. The Activated Complex in Chemical Reactions. *The Journal of Chemical Physics* **3**.2 (1935), 107–115. DOI: 10.1063/1.1749604.

[81] A. A. Arvidsson et al. Metal dimer sites in ZSM-5 zeolite for methane-to-methanol conversion from first-principles kinetic modelling: is the $[Cu–O–Cu]^{2+}$ motif relevant for Ni, Co, Fe, Ag, and Au? *Catal. Sci. Technol.* **7** (7 2017), 1470–1477. DOI: 10.1039/C6CY02521H.

[82] J. S. Woertink et al. A $[Cu2O]^{2+}$ core in Cu-ZSM-5, the active site in the oxidation of methane to methanol. *Proceedings of the National Academy of Sciences* **106**.45 (2009), 18908–18913. ISSN: 0027-8424. DOI: 10.1073/pnas.0910461106.

[83] G. Li et al. Stability and reactivity of copper oxo-clusters in ZSM-5 zeolite for selective methane oxidation to methanol. *Journal of Catalysis* **338** (2016), 305–312. ISSN: 0021-9517. DOI: doi.org/10.1016/j.jcat.2016.03.014.

[84] C. Hammond et al. Direct Catalytic Conversion of Methane to Methanol in an Aqueous Medium by using Copper-Promoted Fe-ZSM-5. *Angewandte Chemie International Edition* **51**.21 (2012), 5129–5133. DOI: 10.1002/anie.201108706.

[85] H. Sjövall, R. J. Blint, and L. Olsson. Detailed kinetic modeling of NH_3 SCR over Cu-ZSM-5. *Applied Catalysis B: Environmental* **92**.1 (2009), 138–153. ISSN: 0926-3373. DOI: 10.1016/j.apcatb.2009.07.020.

[86] J. H. Kwak et al. Excellent activity and selectivity of Cu-SSZ-13 in the selective catalytic reduction of NO_x with NH_3. *Journal of Catalysis* **275**.2 (2010), 187–190. ISSN: 0021-9517. DOI: doi.org/10.1016/j.jcat.2010.07.031.

[87] X. Wang. "Catalytic methane oxidation for emission control and fuel liquefaction". PhD thesis. 2017.

[88] W. Löwenstein. The distribution of aluminum in the tetrahedra of silicates and aluminates. *American Mineralogist* **39** (1/2 1954), 92.

[89] E. Borfecchia et al. Evolution of active sites during selective oxidation of methane to methanol over Cu-CHA and Cu-MOR zeolites as monitored by operando XAS. *Catalysis Today* **333** (2019), 17–27. ISSN: 0920-5861. DOI: 10.1016/j.cattod.2018.07.028.

[90] A. F. Cronstedt. Om En Obekant Bärg Art, Som Kallas Zeolites. *Kongl. Svenska Vetenskaps Academiens Handlingar Stockholm* **17** (1756).

[91] R. Parr and W. Yang. *Density-functional theory of atoms and molecules*. Oxford University Press, 1994.

[92] R. M. Dreizler and E. K. Gross. *Density Functional Theory - An Approach to the Quantum Many-Body Problem*. Springer-Verlag Berlin Heidelberg, 1990. ISBN: 978-3-642-86105-5. DOI: 10.1007/978-3-642-86105-5.

[93] R. Martin. *Electronic Structure: Basic Theory and Practical Methods*. Cambridge University Press, 2004. ISBN: 9780521782852.

[94] P. L. Silvestrelli. Van der Waals Interactions in DFT Made Easy by Wannier Functions. *Phys. Rev. Lett.* **100** (5 Feb. 2008), 053002. DOI: 10.1103/PhysRevLett.100.053002.

[95] E. Bitzek et al. Structural Relaxation Made Simple. *Phys. Rev. Lett.* **97** (17 Oct. 2006), 170201. DOI: 10.1103/PhysRevLett.97.170201.

[96] S. Arrhenius. Über die Dissociationswärme und den Einfluss der Temperatur auf den Dissociationsgrad der Elektrolyte. *Zeitschrift für Physikalische Chemie* **4U**.1 (1889), 96–116. DOI: 10.1515/zpch-1889-0408.

[97] R. Oord, J. E. Schmidt, and B. M. Weckhuysen. Methane-to-methanol conversion over zeolite Cu-SSZ-13, and its comparison with the selective catalytic reduction of NOx with NH3. *Catal. Sci. Technol.* **8** (4 2018), 1028–1038. DOI: 10.1039/C7CY02461D.

[98] D. K. Pappas et al. Methane to Methanol: Structure–Activity Relationships for Cu-CHA. *Journal of the American Chemical Society* **139**.42 (2017), 14961–14975. DOI: 10.1021/jacs.7b06472.